Open access • Journal Article • DOI:10.1533/IJCR.2004.0287

Numerical simulation of the crushing process of composite materials

Silvestre T. Pinho, Pedro P. Camanho, M.F.S.F. de Moura

Institutions: University of Porto

Published on: 01 Jan 2004 - International Journal of Crashworthiness (Woodhead Publishing)

Topics: Advanced composite materials

Numerical Simulation of the Crushing Process of Composite Materials

S.T. Pinho[*], P.P. Camanho [†], M.F. de Moura[‡]

Keywords: Composite materials, crushing, decohesion finite elements.

Abstract

Components in composite materials are progressively replacing metals for crashworthy applications in the automotive, railway and aeronautical industries. The numerical simulation of the crushing process for composite structures is a recent research area. Due to the complex mechanical behaviour of advanced composites, the capability of the existing analytical and numerical models to predict the crushing behaviour of composite materials is still limited.

A numerical model for the crushing simulation of fibre-reinforced composite materials is proposed in this work. The progression of the main cracks is modelled using

[*]DEMEGI, Faculdade de Engenharia, Universidade do Porto, Portugal; currently at the Department of Aeronautics, Imperial College, London, UK

[†]Corresponding author, DEMEGI, Faculdade de Engenharia, Universidade do Porto, Rua Dr. Roberto Frias 4200-465 Porto, Portugal; e-mail:pcamanho@fe.up.pt.

[‡]DEMEGI, Faculdade de Engenharia, Universidade do Porto, Portugal

a new formulation of finite decohesion elements, that allows to correctly account for the energy involved in the crushing process. The intralaminar damage is modelled taking into account the specificities of each material system, degrading the elastic properties in accordance with the different predicted physical damage phenomena.

After the validation of the decohesion element, this concept is used as part of a model for simulation of composite tubes crushing. A good agreement between the numerical results and the experimental data is achieved. The need for further improvements on the physical basis of the intralaminar failure criteria used, as well as on the numerical solution methods for the non-linear problem, is identified.

1 Introduction

Accidents and collisions between vehicles, where human lives are in danger, justify the study of the added-value offered by new structural concepts and new materials for the protection of occupants during crash situations. This field of study, crashworthiness, deals with how materials and structures deform, fail and absorb energy in a controlled form during a crash event. Controlled form means, in this context, a deformation mode where the crushing force is kept to an approximately constant level during the collision, in such a way that a maximum amount of energy is absorbed at bearable levels of acceleration for the passengers.

The composite materials used in crashworthy applications are of polymeric matrix (polyester, epoxy or thermoplastic) strengthened with fibres (typically glass or carbon). The number of applications of structures in composite materials (composite structures) destined to the absorption of energy and consequent protection of

people is already considerable in the aeronautical, automobile and railways industries. The number of applications will certainly continue to grow in the future. This gradual replacement of metallic structures by composite ones is motivated by the higher capacity of energy absorption per unit of weight of the later. The profit in energy absorbed per unit of weight can exceed 500%, in comparison with structures in steel or aluminum [1].

In crushing situations, composites and metals behave very differently. While metals absorb energy by plastic deformation, the process of crushing in composites is more complex. Composites are often constituted by layers and these tend to separate during the crushing (delamination); on the other hand, in each one of these layers, fibre rupture and matrix cracking might take place, either in tensile or compression (intralaminar damage). These damage mechanisms are represented in Figure 1.

(Figure 1 around here)

In the comparison between different geometries and materials for energy absorption, tubular structures—Figure 2a)—are the more often studied in the literature. While easily manufactured, tubes are very similar to the structures in fact used for energy absorption—Figure 2b). Thus, they become a preferred geometry to evaluate and test different lay-up solutions, as well as to validate models, both analytical or numerical. These structures are normally conceived so that a crushing zone progresses in a steady form during the crushing. This destructive zone is located next to the loaded extremity of the tube, and is characterized by the opening of a set of fronds—Figure 2a). During the crushing, the walls of the tube split axially

and delaminate circumferentially. Among the circumferential delaminations, one is distinguished for having the largest dimensions. It is located nearly at half the thickness of the wall and designated as main delamination. In both sides of this delamination, the material form several fronds. These fronds are formed essentially by shear stresses, while the main delamination progresses in an opening mode. The crushing of the material also leads to the formation of a debris wedge between the impacting surface and the tube. This debris wedge remains with an approximately constant size during the process of steady crushing. The friction has an important role, essentially between the surfaces of the fronds and the crushing surface, as well as between the fronds and the debris wedge. During the progression of the crushing process, the tube supports an approximately constant load, whose value determines its capacity of energy absorption—Figure 2c). For this reason, the ability to predict the value of this force is important.

(Figure 2 around here)

The crushing simulation of composites is particularly difficult due to the complexity of its physics. However, the ability to model the crushing and energy absorption of composite structures is particularly important. Indeed, the current knowledge in this field comes from experimental, analytical and numerical sources. The experimental tests suffer from two main limitations: on the one hand, they are rather expensive when one has to model several impact orientations; on the other hand, it is difficult to carry through experimental tests in the initial design stages. Purely analytical models continue to be developed, but its applications are restricted to simple cases. The alternative is therefore numerical modelling. Using numerical models it

is expected to predict the mechanical behaviour of the structures being crushed, as well as a more detailed knowledge of the sequence of events leading to final failure. After developing a numerical model for a specific situation, several crash orientations and impact velocities can be investigated at low cost. This allows to establish response maps, that characterize the structure's crashworthiness. This information can be used iteratively to improve the product, much before manufacturing it.

In the current stage of development, numerical models are still too simplistic to simulate all the mechanical processes relative to the crushing of composite structures. Delamination, for example, is rarely modelled due to the intrinsic numerical difficulties, even though the behaviour of a component is considerably different when delaminated.

In this work, an attempt is made to incorporate a sound physical basis into existing numerical models, allowing for a more realistic simulation of the crushing process. In this context, a tool for delamination modelling has been developed. Meant to be used with the finite element method, a new decohesion element with geometric non-linearity is formulated [2–8]. The geometric non-linearity implemented in this work is necessary to handle the large displacements and rotations that take place during the crushing of composite structures. Indeed, this is essential in applications where structures can undergo important rotations before delaminating. The formulation is implemented in FORTRAN as an 8-noded element and as an 18-noded element, to be used with the software ABAQUS [9]. Furthermore, the intralaminar damage (fibre breaking and matrix cracking in each layer) is also modelled taking into account the specificities of the material being modelled (long aligned fibres/short random

fibres). For long fibres reinfoced composites, the Hashin criterion [10] is accepted as one of the best in describing failure. For short random fibres reinforced composites, several criteria are implemented and compared (maximum stress, maximum strain and Mohr). When the failure criterion is verified, the elastic properties are degraded according to the different predicted damage modes (fibre *or* matrix failure in tension *or* compression). The failure criteria and post-failure behaviour is also implemented in FORTRAN, and ABAQUS software.

After validating the decohesion element, by simulating situations for which there is an analytical solution, the element is included in a numerical model for the simulation of the crushing behaviour of tubular structures. The model comprises, besides the decohesion element, the in-plane failure criteria and elastic properties degradation. It is also shown that the decohesion element is well suited to model the formation and propagation of splitting cracks in the walls of the tubes during the crushing process.

The results obtained through the proposed model are compared with experimental data, and it is concluded that the mean post-crushing load is effectively predicted. The main contributions of this work include:

- formulation and implementation of a decohesion element with geometric non-linearity. This element can be used in several fields, to model delamination, crack propagation and connections between bonded or co-cured components.

- implementation of in-plane failure criteria, and post-failure degradation of the mechanical properties.

- development of a numerical model for crush simulation, based on the previous

contributions. The model is validated and can be used as a tool for the comparison of the crashworthiness value of different materials and geometries; it can also be used to model the crushing of more complex structures, as those represented in Figure 2*b)*.

2 Decohesion element with geometric non-linearity

2.1 Introduction

One of the main limitations in using traditional finite elements to model crack propagation is the problem of mesh dependency. The approach followed in this work to prevent this dependency consists in the use of decohesion elements. The element formulation and implementation is briefly described. Further details are presented in Reference [11].

2.2 Kinematics

(Figure 3 around here)

In a decohesion element—Figure 3*a),* for each point $\mathbf{P}$ in the closed configuration (frequently corresponding to the initial configuration), there are two corresponding points, $\mathbf{P}^-$ and $\mathbf{P}^+$ in any other generic configuration. These two points are designated as *homologous*. A mid point $\mathbf{P^m}$ defined as

$$\mathbf{P^m} = \frac{\mathbf{P}^- + \mathbf{P}^+}{2}. \tag{1}$$

corresponds to each pair of homologous points. The set of all the points $\mathbf{P^m}$ in a element defines its mid surface. Thus, designating by $\mathbf{r}$ the updated position vector

of a point in the middle surface, by $\mathbf{x}$ its initial position vector, by $\mathbf{u}^+$ and $\mathbf{u}^-$ the displacements of the (considered) top and bottom surfaces, the *i-th* coordinate of the middle surface can be written:

$$r_i = x_i + \frac{1}{2}(u_i^- + u_i^+). \tag{2}$$

The relative displacement between two points $\mathbf{P}^+$ and $\mathbf{P}^-$ is, for the coordinate i,

$$\Delta_i = u_i^+ - u_i^-. \tag{3}$$

The displacements $u_i^+$and u_i^- are obtained through interpolation of the nodal values u_{ki}, resulting for Δ_i

$$\Delta_i = u_i^+ - u_i^- = \overline{N}_k u_{ki} \tag{4}$$

where $\overline{N}_k$ are shape functions. For fracture mechanics applications, it is convenient to express the relative displacement in a local coordinate system—(ξ, η, ζ) , Figure 3 *b)*—as an opening and two sliding modes. The relative displacement in a local coordinate system, δ_s, is obtained through the displacement in the global coordinate system, Δ_i, and a transformation tensor θ_{si} :

$$\delta_s = \theta_{si}\Delta_i. \tag{5}$$

Finally, defining $B_{sik} = \theta_{si}\overline{N}_k$, the expression for the relative displacement in the local coordinate system as a function of the nodal displacements (in a global coordinate system) is written as

$$\delta_s = B_{sik}u_{ki}. \tag{6}$$

2.3 Constitutive law

In the local coordinate system, the relative displacements, δ_r, are related to the tractions acting on the surfaces by the constitutive law

$$\tau_s = D_{sr}\delta_r. \tag{7}$$

(Figure 4 around here)

The generic shape of the constitutive law for pure opening or pure shear behaviour is presented in Figure 4*a)*, while the mixed-mode behaviour is presented in Figure 4*b)*. For pure mode loading, the traction τ_i increases with the relative displacement δ_i up to a maximum value N, S or T (according to the mode) and then decreases to zero.

For mixed-mode situations, a stress-based interaction criterion is used for damage initiation at the interface:

$$\left(\frac{\tau_1}{S}\right)^2 + \left(\frac{\tau_2}{T}\right)^2 + \left(\frac{\langle\tau_3\rangle}{N}\right)^2 = 1 \tag{8}$$

where $\langle x\rangle$ is the McCauley operator defined as $\langle x\rangle = \frac{1}{2}\left(x + |x|\right)$.

This criterion has been shown by other authors [6],[12] to be in good agreement with experimental data. The area under the traction-displacement curve—i.e. the energy absorbed during failure at that point—in a mixed mode situation is defined by an energy-based interaction criterion. Two different criteria are implemented. The power law criterion [13, 14]

$$\left(\frac{G_I}{G_{IC}}\right)^\alpha + \left(\frac{G_{II}}{G_{IIC}}\right)^\alpha = 1 \tag{9}$$

and the B-K criterion [15]

$$G_{IC} + (G_{IIC} - G_{IC}) \left(\frac{G_{II}}{G_I + G_{II}} \right)^{\eta} = G_I + G_{II}. \tag{10}$$

The parameter α in the power law criterion and the parameter η in the B-K can be regarded as material properties that reflect how mode I and mode II interact in a mixed-mode situation.

2.4 Equilibrium of the element

The virtual work method is applied to derive the stiffness tensor of the element

$$K_{kizv} = \int_A D_{sr} B_{rvz} \left(\frac{\partial B_{spy}}{\partial u_{ki}} u_{yp} + B_{sik} \right) dA, \tag{11}$$

and the equilibrium of the element can thus be expressed as

$$K_{kizv} u_{zv} = f_{ki}. \tag{12}$$

However, this is a geometric and material non-linear problem. As a result, incremental iterative methods, such as Newton-Raphson and Riks, are the most suited for its resolution. Therefore, the tangent stiffness tensor K^T_{kizv} defined by the differentiation of Equation 12 is necessary to achieve fast convergence, especially in more complicated problems:

$$K^T_{kizv} du_{zv} = df_{ki} \tag{13}$$

The full mathematical deduction of the expression for the tangent stiffness tensor is presented in Reference [11].

2.5 Validation of the decohesion element - MMB test

The decohesion element is used to simulate the delamination in a MMB test (Mixed Mode Bending [16]) and a comparison with the analytical solution is carried to validate the element. The specimen geometry and loading are presented in Figure 5*a)*.

(Figure 5 around here)

The value of the lever length c—Figure 5*a)*—is used to define the relative contribution of mode I and mode II. The specimen has typical properties for a carbon/PEEK material. The Young modulus is 1.5×10^5 N/mm^2 and the Poisson ratio is 0.33. The geometric parameters and the properties of the interface are shown in Table 1.

(Table 1 around here)

Figure 5*b)* presents the numerical and analytical load-displacement curves for this specimen. The small difference in the elastic region is due to a unreallystic assumption in the analytical curve[1]. For the region corresponding to crack propagation, the agreement obtained is excellent. This result (with others for pure mode I and II presented in Reference [11]) prove the suitability of the element to model crack propagation regardless of the mode ratio.

3 In-plane failure criteria

The criteria presented in this section are expressed as functions (f) of the components of the stress tensor and of the ply strengths.

[1] the analyitical solution neglets the rotation of the specimen's arms at the crack tip

3.1 Layers reinforced with continuous fibres

For layers reinforced with continuous fibres, the Hashin criterion [10] has the advantage of distinguishing between different failure modes. For a three-dimensional situation, it is expressed as:

fibre tensile failure

$$f_f{}^t = \left(\frac{\sigma_1}{X_t}\right)^2 + \left(\frac{\sigma_{12}+\sigma_{13}}{S_\sigma}\right)^2 \qquad , \qquad \sigma_1 \geq 0 \tag{14}$$

fibre compressive failure

$$f_f{}^c = \frac{-\sigma_1}{X_c} \qquad , \qquad \sigma_1 < 0 \tag{15}$$

matrix tensile cracking

$$f_m{}^t = \left(\frac{\sigma_2+\sigma_3}{Y_t}\right)^2 + \frac{\sigma_{12}^2+\sigma_{13}^2+\sigma_{23}^2-\sigma_2\sigma_3}{S_\sigma^2} \qquad , \qquad \sigma_2+\sigma_3 \geq 0 \tag{16}$$

matrix compression cracking

$$f_m{}^c = \left(\frac{\sigma_2}{2S_\sigma}\right)^2 + \left(\frac{\sigma_{12}}{S_\sigma}\right)^2 + \left[\left(\frac{Y_c}{2S_\sigma}\right)^2 - 1\right]\frac{\sigma_2}{Y_c} \qquad , \qquad \sigma_2+\sigma_3 < 0 \tag{17}$$

In Equations 14-17, σ_i represent normal stresses, σ_{ij} represent shear stresses; X_t and X_c represent the strength in the fibre direction (traction and compression); Y_t and Y_c represent the strength in the transverse direction (traction and compression); S_σ is the in-plane shear strength.

3.1.1 Effect of damage in the elastic properties

When failure is detected (Equations 14-17), some material properties are affected. Based on existing micromechanical analyses, [17–19], Camanho *et al.* [20] have proposed the following reduction, used in this work:

matrix tensile cracking

$$E_2^d = 0.2E_2,\ G_{12}^d = 0.2G_{12} \quad \text{and} \quad G_{23}^d = 0.2G_{23} \tag{18}$$

fibre tensile failure

$$E_1^d = 0.07E_1 \tag{19}$$

matrix compression cracking

$$E_2^d = 0.4E_2, \quad G_{12}^d = 0.4G_{12} \quad \text{and} \quad G_{23}^d = 0.4G_{23} \tag{20}$$

fibre compressive failure

$$E_1^d = 0.14E_1 \tag{21}$$

where E_i is the Young modulus in the i direction and G_{12} is the shear modulus; the upper index d represents damaged mechanical property.

3.2 Layers reinforced with short random fibres

For composites reinforced with short random fibres, three different criteria are implemented and compared:

Maximum strain

$$f = \max\left(\frac{\langle \varepsilon_{P1} \rangle}{X_{\varepsilon t}}, \frac{\langle -\varepsilon_{P3} \rangle}{X_{\varepsilon c}}, \left|\frac{\varepsilon_{shear}^{\max}}{S_\varepsilon}\right|\right) \tag{22}$$

Maximum stress

$$f = \max\left(\frac{\langle \sigma_{P1} \rangle}{X_t}, \frac{\langle -\sigma_{P3} \rangle}{X_c}, \left|\frac{\tau^{\max}}{S_\sigma}\right|\right) \tag{23}$$

Mohr

$$f = \frac{\langle \sigma_{P1} \rangle}{X_t} + \frac{\langle -\sigma_{P3} \rangle}{X_c} \tag{24}$$

where ε_{Pi} (σ_{Pi}) represent the *i-th* principal strain (stress); $X_{\varepsilon t}$ and $X_{\varepsilon c}$ maximum strains (traction and compression); $\varepsilon_{shear}^{\max}$ and $\tau^{\max}$ are the maximum shear strain and stress; and S_ε is the maximum shear strain.

3.2.1 Effect of damage in the elastic properties

When failure is detected, the elastic properties are degraded according to

$$E^d = DE \tag{25}$$

$$G^d = DG \tag{26}$$

where the damage variable D should ideally be obtained from experimental data or micromechanical models. In the absence of those, its value should be realistic, i.e., the elastic properties should be reduced according to the real, experimental material behaviour. Furthermore, in an implicit finite element analysis, there are some restrictions to the magnitude in the reduction of the elastic properties, for numerical reasons. Tay *et al.* [21] refer that in a tube crush simulation, convergence was not achieved for reductions higher than 50%. Johnson and Picket [22] refer that the numerical instabilities are too accentuated for reductions higher than 90%. In this work, the values $D = 0.1$ and $D = 0.15$ are used (corresponding to reductions of 85 and 90%).

4 Crushing simulation

The numerical model developed is applied to five different tube crushing situations. Experimental data for all these cases is available in published literature. The simulations use the decohesion element to model delamination and propagation of the main cracks in the tube walls (axial splitting), as well as the intralaminar failure criteria previously presented.

4.1 Carbon/PEEK - continuous fibres

Hamada *et al.* present in Reference [23] the results of an experimental work on tube crushing. The authors used carbon/PEEK (AS4/APC-2) with 20 layers, being the fibres aligned with the cylinder's axe. The mean diameter of the tube is 55 mm and the wall thickness is 2.66 mm. The elastic properties are presented in Table 2.

(Table 2 around here)

Some properties needed for the proposed numerical model are not specified by Hamada *et al.* [23]. In these cases, typical values for the corresponding material were used, as specified in Table 3; the mode I and mode II energy release rates are respectively 0.28 and 1.42 N/mm. Following work from Mamalis *et al.* [24] the value of the friction coefficient used is 0.3. Possible models simulating the tests of Hamada *et al.* [23] could aim at simulating the stable crush propagation, or at simulating the peak forces during initiation (see Figure 6). Modelling both aspects with only one model is bound to be a very difficult task, due to the considerable geometric transformations during initiation. For its relevance in terms of the energy absorbed, the model developed in this work is applied to crush propagation—Figure 6 *f)*.

(Figure 6 around here)

The three-dimensional model for this case intends to simulate the splitting of the cylinder into several fronds, the main delamination that opens the wall in two, and the intralaminar damage (fibre breaking and matrix cracking). Taking into account the experimental observation that the tube splits into 12 approximately equal fronds, only $1/12^{th}$ of the tube is modelled, corresponding to half of two consecutive fronds (and the crack between them, see Figure 7). Decohesion elements are used in the boundary between the two fronds that are formed in the experimental tests, in order to simulate their formation. More decohesion elements are used at half the thickness of the wall, to model the main delamination. Furthermore, Hashin's criterion is used for the intralaminar damage, with the degradation of the elastic properties presented in section 3. In the simulation, the impacting surface includes already the debris wedge resulting from initiation, as well as the bend layers at the top. Figure 7 shows the mesh of the specimen, as well as the impacting surface, in the initial and a deformed configuration.

(Figure 7 around here)

For the boundary conditions, the bottom part of the tube is fixed, and appropriated symmetry conditions are applied to the central part of each frond. The central part of each frond corresponds to the left and right ends (two planes) in the finite element mesh. A symmetry condition relative to that plane is applied to each node in these planes.

A displacement is applied to the (rigid) impacting surface. Figure 7 presents the crushing evolution.

Intralaminar damage also occurs during the crushing. Figure 8 presents the different damage modes at a fixed moment.

(Figure 8 around here)

(Figure 9 around here)

(Table 4 around here)

Figure 9 and Table 4 present the main results. The numerical results obtained by Tay *et al.* [21] and by the present model are compared to the experimental mean post-crushing load obtained by Hamada *et al.* [23] in Figure 9*a)*. In the present model, two different tube lengths are considered: $L = 40\,\mathrm{mm}$ and $L = 100\,\mathrm{mm}$. It can be concluded that the post-crushing load is not affected by the length of the tube. The initial elastic stiffness in the decohesion element formulation (penalty) is known to be a critical parameter on what concerns convergence capability, and is therefore studied in more detail. Several values are compared: $K = 10^6 \mathrm{N/\,mm^3}$, $K = 10^5 \mathrm{N/\,mm^3}$ and $K = 10^4 \mathrm{N/\,mm^3}$ (K6, K5 and K4 in Figure 9*b)*). It can be concluded from 9*b)* that reducing the penalty value increases the convergence capability of the model. Furthermore the mean post crushing load is predicted with considerable accuracy, even though there is a limited convergence capability during the crushing process.

4.2 Glass/polyester - short random fibres

Mamalis *et al.* [24] carried a comprehensive experimental work on the crushing behaviour of glass/polyester tubes. The dimensions of three specimens types tested by Mamalis are here designated as Case 1, Case 2 and Case 3, and are presented in

Table 5. The experimental mean post crushing load for these cases is 33.5, 41.6 and 62.4 kN respectively.

(Table 5 around here)

(Table 6 around here)

The mechanical properties are presented in Table 6. The friction coefficient used is also 0.3.

Several simulations are carried, differing mainly in (i) the failure criterion: the Mohr, maximum stress and maximum strain criteria are compared; (ii) the influence of damage in the elastic properties, where residual stiffness values of 10% and 15% of the initial one are considered. It should be noticed that there are limitations on the amount of reduction to the elastic properties possible in numerical simulations [21, 22].

4.2.1 Case 1

The numerical model includes the debris wedge, just like in the previous case analysed. Figure 10 shows both the mesh and the impacting surface. The results obtained with the Mohr (M-C), maximum stress (Mσ) and maximum strain (Mε) criteria for 10% residual stiffness are presented in Figure 11 and Table 7. Considering that the convergence capability for the Mohr and maximum strain failure criteria is not very good, simulations for these two criteria with 15% residual stiffness, are also presented in Figure 11 and Table 7.

(Figure 10 around here)

(Figure 11 around here)

(Table 7 around here)

4.2.2 Case 2

As mentioned previously, Case 2 differs from Case 1 on what concerns to the dimensions of the specimen. The numerical model is thus in this case very similar to the one presented for Case 1. The Mohr, maximum stress and maximum strain criteria are also compared for this type of specimen. The residual strength is 10% of the initial and the penalty values $K = 10^6 \text{N/mm}^3$ (K6) and $K = 10^5 \text{N/mm}^3$ (K5) are compared. The numerical results obtained are presented in Figure 12 and Table 8.

(Figure 12 around here)

(Table 8 around here)

4.2.3 Case 3

As mentioned, Case 3 specimens differ from Case 1 and Case 2 specimens only on what concerns the dimensions. The residual strength is also considered to be 10% of the initial. The Mohr, maximum stress and maximum strain criteria are again compared. Three different values for the penalty are compared: $K = 10^6 \text{N/mm}^3$, $K = 10^5 \text{N/mm}^3$ and $K = 10^4 \text{N/mm}^3$ (K4). The effect of decreasing the maximum traction in the delamination of the wall to 10MPa (S10) is also investigated, for the Mohr failure criterion. The numerical results are presented in Figure 13 and Table 9.

(Figure 13 around here)

(Table 9 around here)

4.3 Glass/polyester - Continuous fibres

Abdel-Haq *et al.* [25] crushed pultruded glass/polyester tubes, with properties shown in Table 10. Figure 14 shows the tube and the impacting surface used. The inner diameter is 44 mm and the wall thickness is 3 mm. The radius of the curved part of the crushing surface is 12 mm.

(Table 10 around here)

(Figure 14 around here)

The tube opened in 6 fronds, Figure 14. The inner-upper edge crushed due to the contact stresses—Figure 14*a)*—and, later on the crushing process, the wall delaminated, Figure 14*b)*.

This is a particularly interesting case study for the validation of a numerical model for crush simulation, since it allows to model the initiation and damage propagation in the same run. This is due to the small changes in the geometry during the initiation. Indeed, no debris wedge is formed, and only the inner-top edge is crushed.

The model used for the simulation is shown in Figure 14*a)*. and *b)*. Note that the inner-top edge of the tube is not included, as it was crushed in the early phase of the crushing process. Furthermore, the existing symmetry is considered, and only half of two consecutive fronds are modelled. The mechanical properties shown in Table 10 are used. Following the results from References [26, 27] the energy release rates for mode I and II are 0.2 and 0.5kJ/m^2. The penalty value used is $K = 10^5$N/mm^3. Several simulations with coefficients of friction $\mu = 0.4$, 0.5 and 0.6 are carried, since several test results from Mamalis *et al.* [24] suggest that the coefficient of friction lies

in the range 0.3-0.7. The Hashin failure criterion is considered for the intralaminar damage.

Figures 15*c)* and 16 shows the frond formation (i.e. axial splitting), which is very similar to the experimental (Figure 14). Figure 16 shows the mode II delamination in the wall of the tube. This delamination can also be observed in the tests—Figure 14. From a numerical point of view, it is interesting to note that the decohesion elements allows to model this delamination and the contact between the fronds, even though they are rotated from their original position. This could not be achieved without the non-linear formulation implemented.

(Figure 15 around here)

(Figure 16 around here)

Figure 17 compares the results obtained with different friction coefficients. The general shape of the numerical load-displacement curves is in good agreement with the experimental one. Other results [11] indicate that the small oscillations in the region corresponding to 3-8mm displacement are related to the mesh size. Table 11 compares quantitatively the error in that region for all the simulations. The friction coefficient is confirmed to have a great influence on the structural response, as already observed by other authors [24].

(Figure 17 around here)

(Table 11 around here)

5 Conclusions

The simulation of the crushing behaviour of composite structures is of great importance for the automotive, railway and aerospace industries. Indeed, the survival of passengers in crash situations depends on the mechanical behaviour of the crashworthy components present in the vehicles. The development of crashworthy components should be accomplished using numerical simulation as a part of the design process.

Crushing of composite components is a physically complex phenomenon. Several factors contribute for this, among which these can be mentioned: (i) great difference of scale between the typical wall thickness and other dimensions of the components; (ii) the great displacements and rotations involved, requiring the use of non-linear geometric analyses; (iii) the different mechanisms of damage, and material non-linearities; (iv) deep geometric transformations in the crushing zone; (v) the contact and (vi) the friction.

The approach followed in this work consists on: (i) modelling the progression of the main macro-cracks (main delamination and axial splitting of the wall) using decohesion elements, with a formulation that uses a traction/relative-displacement constitutive law, introducing a non-linear geometric formulation, which allows to correctly account for the energy consumed during crack propagation; (ii) using an intralaminar damage model (adapted for each type of material considered) to simulate the deterioration caused by each damage mode predicted (fibre breaking and matrix cracking, in tensile and compression); (iii) to use an implicit finite element method, which correctly solves the equilibrium equations.

The proposed numerical model is used to predict the post-crushing load in composite tubes. The deep geometric transformations that often take place in the crushing zone during the initial crushing stages—and result in the formation of a debris wedge—are directly included in the models. Different material systems (Carbon/PEEK and Glass/Polyester) and different fibre architectures (continuous fibres and random short fibres) are modelled. In most cases, the model predicts the post-crushing load within an error of 10%, even though the error values have occasionally reached about 20%. Given the complexity of the physical process simulated, this error magnitude can be considered good for this type of problems. The error in the prediction of the post-crushing load results from the combination of several factors: (i) the values of the properties introduced (in some cases, those properties are only typical values for the material system under consideration), (ii) simplifications implicit in the model (for instance, not all the interfaces on the wall of the tubes are modelled); (iii) the intralaminar failure models are only approximations for the real material behaviour and finally (iv) discretization and numerical errors in general.

For glass/polyester composites, with short random fibres, the Mohr criterion proves to be more adequated than the Maximum Stress and the Maximum Strain criteria for all three cases studied. For long aligned fibre composites, either carbon/PEEK or glass/polyester, the Hashin criterion proves to be well suited. Residual strength values of about 10% of the original values seem to correctly represent the real material behaviour, and are in the limit range of values for which convergence under an implicit solution can still be achieved. The penalty value of the decohesion elements (i.e. the elastic 'stiffness') and the maximum stress at onset of

damage are shown to significantly affect the convergence capability of the models, without considerable effect on the post-crushing load.

In one case, the model was used to simulate all the crushing process, including initiation. The correlation with the experimental results during the elastic and the damage evolution phases, is a remarkable proof that the most relevant physical aspects are incorporated in the model.

The proposed model is thus in a phase where it can be used directly in the design of tubes for crashworthiness applications, or even in more complex crashworthy components. It can also be used to compare different material systems or reinforcement architectures.

The main limitations associated with the proposed model are related to its convergence capabilities. Hence, further work in this field should focus on this particular aspect. More specifically, further work should be carried on: (i) the form of the constitutive law of the interface element (polynomial, instead of bilinear); (ii) the solution scheme for the equilibrium equations (in this work, the Riks method was used as it proved to be the best suited in these problems, from those available on ABAQUS); and (iii) the exploitation of the possible advantages of explicit formulations. Another aspect that should deserve some attention on future research is the physical basis of the intralaminar failure criteria used, as well as the micromechanics of damage propagation.

References

[1] S Ramakrishna. Microstructural design of composite materials for crashworthy structural applications. *Materials and Design*, 18:167–173, 1997.

[2] M F S F de Moura, J P Gonçalves, A T Marques, and P T de Castro. Elemento finito isoparamétrico de interface para problemas tridimensionais. *Revista Internacional de Métodos Numéricos Para Cálculo e Diseño en Ingeniería*, 14:447–466, 1996.

[3] M F S F de Moura, J P Gonçalves, A T Marques, and P T de Castro. Modeling compression failure after low velocity impact on laminated composites using interface elements. *Journal of Composite Materials*, 31:1462–1479, 1997.

[4] M F S F de Moura, J P Gonçalves, A T Marques, and P T de Castro. Prediction of compressive strength of carbon-epoxy laminates containing delaminations by using a mixed-mode damage model. *Composite Structures*, 50:151–157, 2000.

[5] J P Gonçalves, M F S F de Moura, P M S T de Castro, and A T Marques. Interface element including point-to-surface constraints for three-dimensional problems with damage propagation. *Engineering Computations*, 17(4):28–47, 2000.

[6] P P Camanho, C G Dávila, and D R Ambur. Numerical simulation of delamination growth in composite materials. Technical Report TP-2001-211041, NASA, 2001.

[7] P P Camanho and M F de Moura. Simulation of interlaminar damage using decohesion elements. In *13th Interantional Conference on Composite Materials*, Beijing, China, 2001.

[8] P P Camanho and C G Dávila. Mixed-mode decohesion finite elements for the simulation of delamination in composite materials. Technical Report TM-2002-211737, NASA, 2002.

[9] ABAQUS Users Manual. *Version 6.1.* Hibbit, Karlsson and Sorensen Inc., 2000.

[10] Z Hashin. Failure criteria for unidirectional fibre composites. *Journal of Applied Mechanics*, 47:329–334, 1980.

[11] S T Pinho. Simulation of the crushing behaviour of composite structures. Master's thesis, University of Porto, Faculty of Engineering, 2002. In Portuguese.

[12] C G Dávila, P P Camanho, and M F de Moura. Mixed-mode decohesion elements for analyses of progressive delamination. In *42nd AIAA/ASME/ASCE/AHS/ASC Structures, Structural Synamics, and Materials Conference and Exhibit*, Seattle, USA, 2001.

[13] Y Mi, M A Crisfield, and A O Davies. Progressive delamination using interface elements. *Journal of Composite Materials*, 32(14):1246–1272, 1998.

[14] E M Wu and R C Jr Reuter. Crack extension in fibreglass reinforced plastics. Technical Report no. 275, T and AM, University of Illinois, 1965.

[15] M L Benzeggagh and M Kenane. Measurement of mixed-mode delamination fracture toughness of unidirectional glass/epoxy composites with mixed-mode bending apparatus. *Composites Science and Technology*, 56(4):439–449, 1996.

[16] American Society for Testing and Materials. Test method d6671-01, standard test method for mixed mode i-mode II interlaminar fracture toughness of unidirectional fiber reinforced polymer matrix composites, 2001.

[17] R J Nuismer and S C Tan. Constitutive relations of a cracked composite lamina. *Journal of Composite Materials*, 22:306–321, 1988.

[18] S C Tan and R J Nuismer. A theory for progressive matrix cracking in composite laminates. *Journal of Composite Materials*, 23:1029–1047, 1989.

[19] S C Tan and J Perez. Progressive failure of laminated composites with a hole under compressive loading. *Journal of Reinforced Plastics and Composites*, 12:1043–1057, 1993.

[20] P P Camanho and F L Matthews. A progressive damage model for mechanically fastened joints in composite laminates. *Journal of Composite Materials*, 33:2248–2280, 2000.

[21] T E Tay, K H Lee, S Ramakrishna, and F Shen. Modelling the crushing behaviour of composite tubes. *Key Engineering Materials*, pages 777–790, 1998.

[22] A Johnson and A K Pickett. Impact and crash modelling of composite structures: A challenge for damage mechanics. In *European Conference on Computational Mechanics, ECCM'99*, Munich, Germany, 1999.

[23] H Hamada and Ramakrishna. Scaling effects in the energy absorption of carbon-fiber/PEEK composite tubes. *Composites Science and Technology*, 55:211–221, 1995.

[24] A G Mamalis, D E Manolakos, G A Demosthenous, and M B Ioannidis. *Crashworthiness of Composite Thin-Walled Structural Components*. Technomic, Lancaster, PA, 1998, 1998.

[25] M Abdel-Haq, G B Broggiato, and G M Newaz. Constrain effects on energy absorption in unidirectional PMC tubes. *Journal of Composite Materials*, 33(9):74–793, 1999.

[26] F Ozdil and L A Carlsson. Beam analysis of angle-ply end-notched flexure specimens. *Composites Science and Technology*, 58:1929–1938, 1998.

[27] F Ozdil and L A Carlsson. Beam analysis of angle-ply laminate DCB specimens. *Composites Science and Technology*, 59:305–315, 1999.

[28] P P Camanho. *Application of Numerical Methods to the Strength Prediction of Mechanically Fastened Joints in Composite Laminates*. PhD thesis, Imperial College of Science and Technology, 1999.

[29] G L Farley. Relationship between mechanical property and energy absortion trends for composite tubes. Technical Report NASA-TP-3284, ARL-TR-29, Vehicle Structures Directorate, U. S. Army Research Laboratory, Langley Research Center, NASA, 1993.

Tables

Table 1: Geometric parameters and properties of the interface for the MMB specimen

Geometry (mm)		Interface properties	
length	100	K	10^6 N/mm^3
initial crack	30	G_{IC}	0.28 N/mm
thickness	3	G_{IIC}	1.42 N/mm
width	10	N	30 N/mm^2
c	43.7	S	40 N/mm^2

Table 2: Elastic properties for carbon/PEEK (AS4/APC-2), from Hamada *et al.* [23]

E_1 (GPa)	$E_2 = E_3$ (GPa)	$\nu_{12} = \nu_{13}$	ν_{23}	$G_{12} = G_{13}$ (GPa)	G_{23} (GPa)
139	10	0.26	0.03	4.5	1.3

Table 3: Strength of carbon/PEEK (AS4/APC-2), from [8]

X_t	X_c	Y_t	Y_c	S_{12}	$Z_{t/c} = S_{13} = S_{23}$
(MPa)	(MPa)	(MPa)	(MPa)	(MPa)	(MPa)
2070	2070	90	160	115	90

Table 4: Current numerical results and comparison with References [21, 23]

	Mean post crushing load $\bar{P}$ (kN)	Error
Experimental (Hamada, 1995)	110.7	–
3D implicit model (Tay, 1998)	149.5	35.1%
Proposed model ($L = 40$ mm; $K = 1E6$ N/mm^3)	104.6	−5.5%
Proposed model ($L = 100$ mm; $K = 1E6$ N/mm^3)	103.9	−6.1%
Proposed model ($L = 40$ mm; $K = 1E5$ N/mm^3)	109.1	−1.4%
Proposed model ($L = 40$ mm; $K = 1E4$ N/mm^3)	117.6	6.2%

Table 5: Dimensions of the tubes tested by Mamalis *et al.* [24]

Case	1	2	3
Number of layers	3	4	5
Thickness t_p (mm)	3.4	4.4	5.7
Mean diameter $\bar{D}$ (mm)	55.0	57.0	61.2

Table 6: Mechanical properties of the specimens testd by Mamalis *et al.* [24]

E (GPa)	X_t (MPa)	G_{IC} (kJ/m^2) (Delamination)	G_{IC} (kJ/m^2) (Wall)	K N/mm^3
9	180	0.11	0.2	1E6

Table 7: Numerical results for Case 1 and comparison with Reference [24]

	Post-crushing load, $\bar{P}$ (kN)	Error
Experimental, Case 1 (Mamalis, 1998)	33.5	–
M-C, 10%	34.5	2.8%
M-C, 15%	36.1	7.7%
Mσ, 10%	34.8	3.9%
Mε, 10%	29.3	−12.6%
Mε, 15%	31.6	−5.6%

Table 8: Present numerical results for Case 2, and comparison with Reference [24]

	Post-crushing load, $\bar{P}$ (kN)	Error
Experimental, Case 2 (Mamalis, 1998)	41.6	–
M-C, K5	48.2	15.9%
M-C, K6	47.8	15.0%
Mσ, K6	52.0	24.9%
Mε, K6	32.8	−21.2%

Table 9: Present numerical results for Case 3, and comparison with Reference [24]

	Post-crushing load, $\bar{P}$ (kN)	Error
Experimental, Case 3 (Mamalis, 1998)	62.4	–
M-C, K4	66.3	6.2%
M-C, K5	66.9	7.3%
M-C, K6	64.6	3.5%
M-C, K6, S10	66.0	5.8%
Mσ, K5	73.4	17.7%
Mσ, K6	70.9	13.7%
Mε, K5	55.9	−10.5%
Mε, K6	56.1	−10.1%

Table 10: Mechanical properties of the glass/polyester tubes tested by Abdel-Haq *et al.* [25]

E_1	E_2	G_{12}	ν	X_t	Y_t	X_c	Y_c	S_{12}
(GPa)	(GPa)	(GPa)		(MPa)	(MPa)	(MPa)	(MPa)	(MPa)
17	5.4	2.9	0.33	204	48	204	102	50

Table 11: Present numerical results, and comparison with Habdel-Haq *et al.* [25]

	Post-crushing load, $\bar{P}$ (kN)	Error
Experimental [25]	3.86	–
$\mu = 0.4$	3.09	-19.9%
$\mu = 0.5$	3.31	-14.3%
$\mu = 0.6$	3.67	-4.8%

Figures

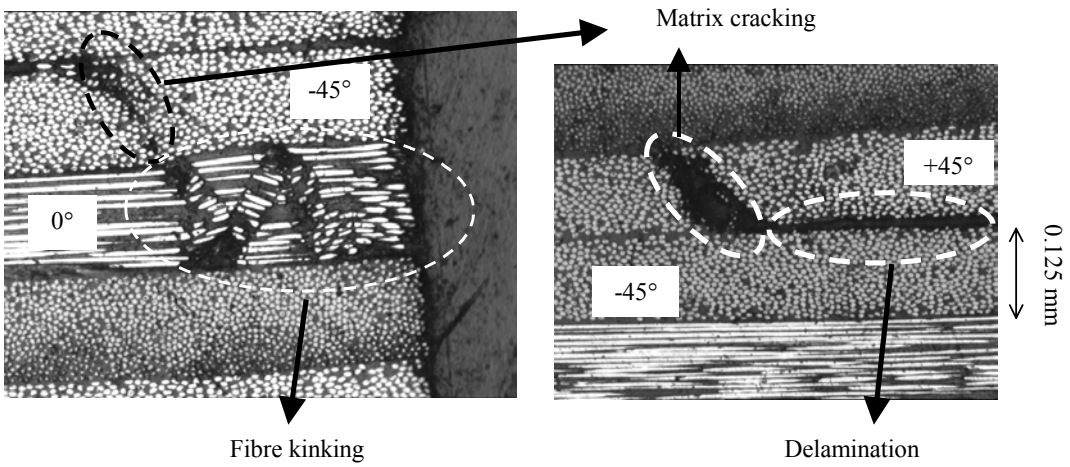

Figure 1: Different failure mechanisms in composites, from [28]

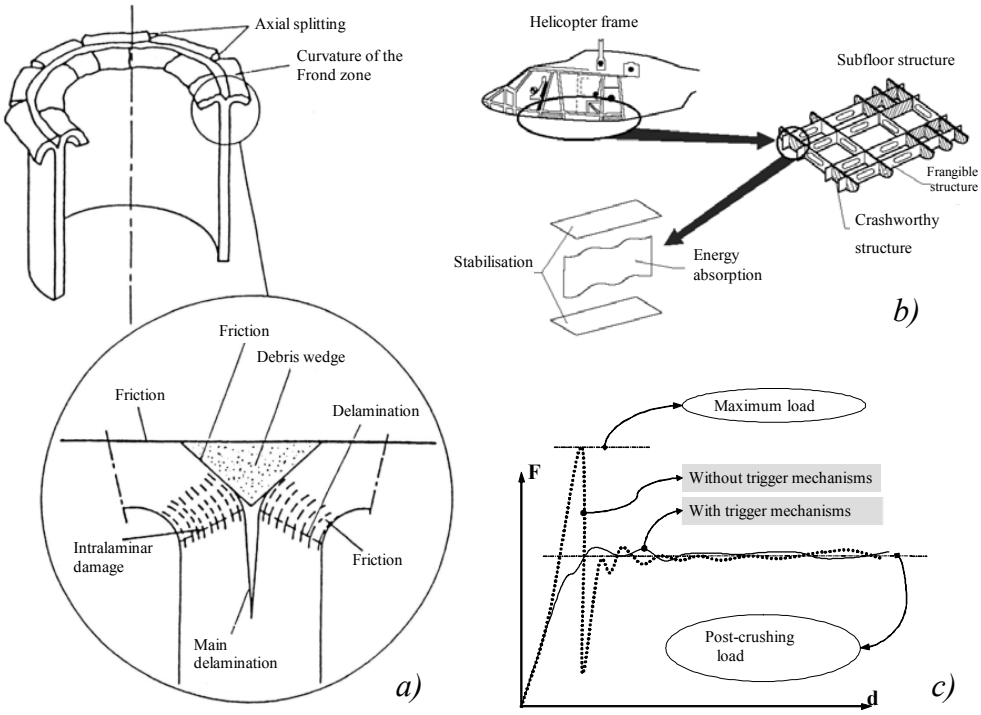

Figure 2: *a)* Crushing of a composite tube, after [24]; *b)* real structure for energy absorption, after [29]; *c)* typical load-displacement curve

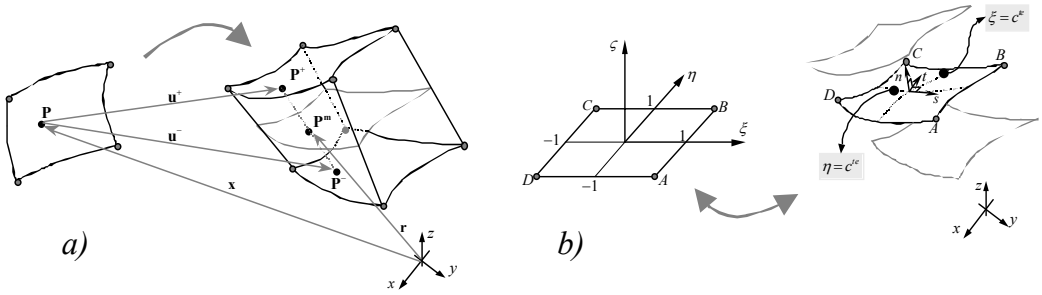

Figure 3: *a)* Decohesion element in a closed and generic configuration; *b)* global and local coordinate systems

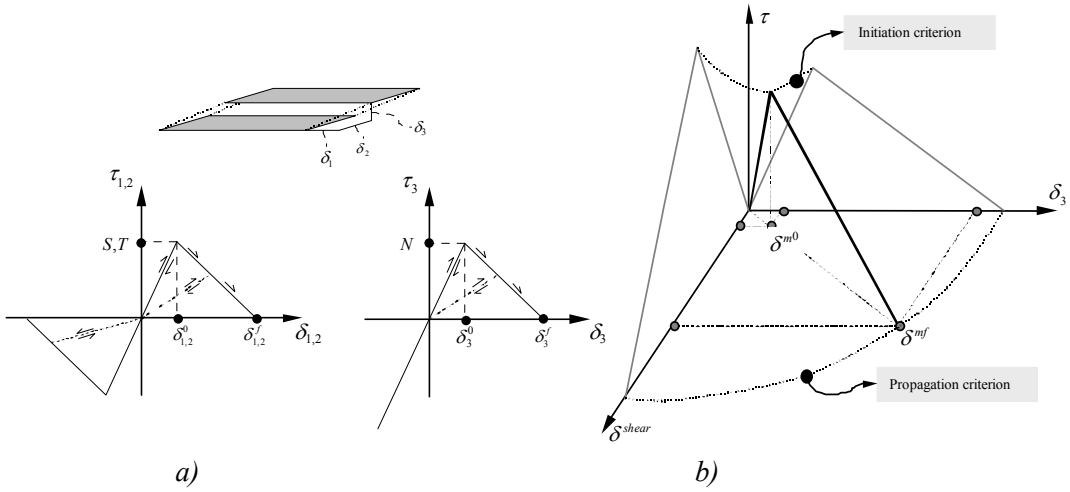

Figure 4: Constitutive law for the decohesion element: *a)* pure opening and shear modes, *b)* mixed mode

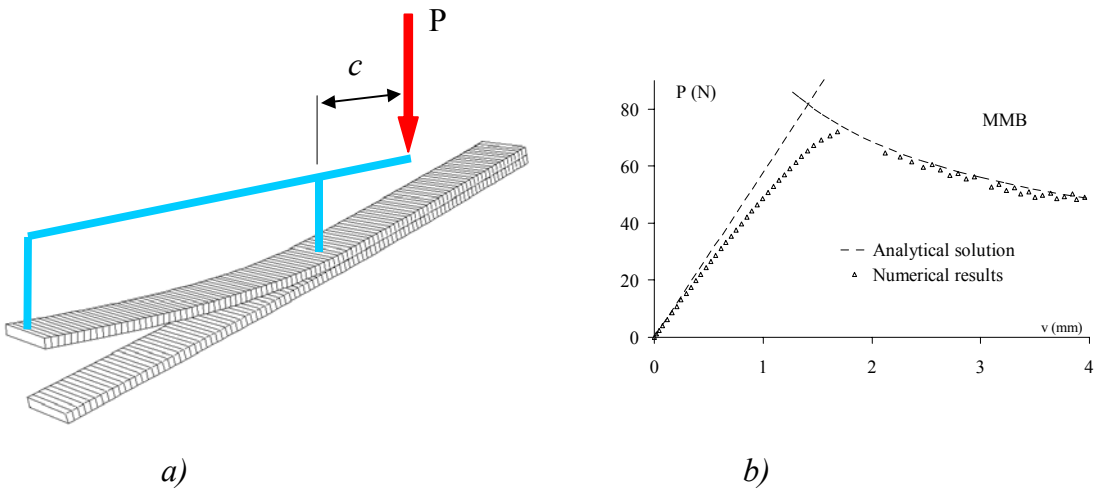

Figure 5: *a)* Finite element mesh; *b)* load-displacement curve

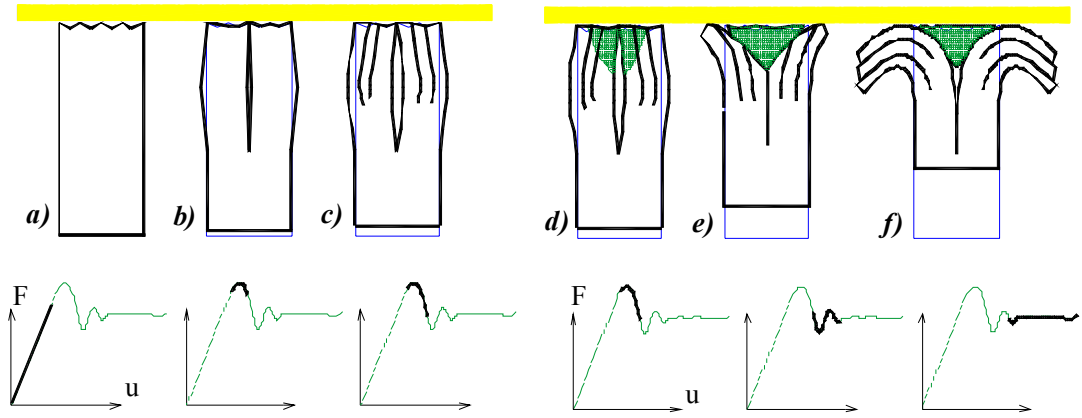

Figure 6: Consecutive crushing stages

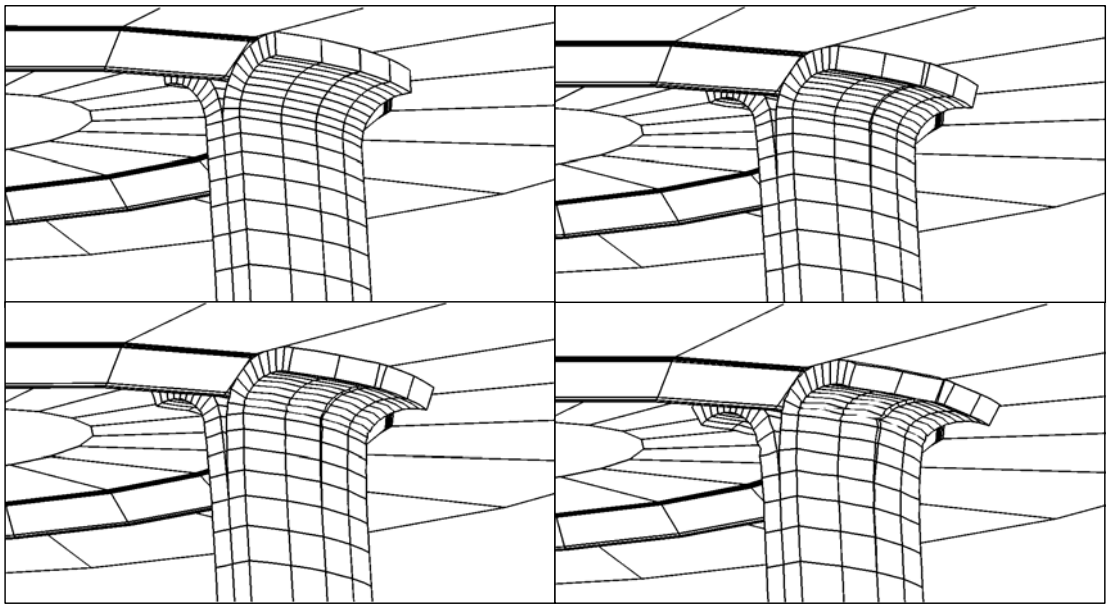

Figure 7: Crushing progression showing opening of the fronds and the evolution of the main delamination

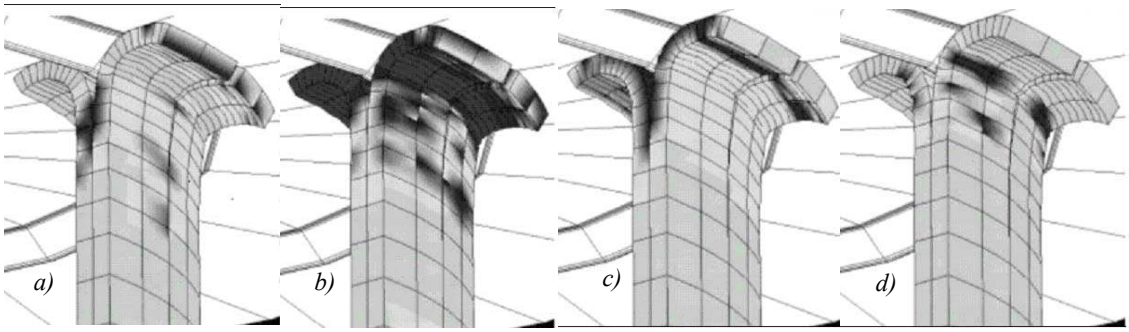

Figure 8: Damage modes (dark regions): *a)* matrix tensile cracking; *b)* matrix compressive cracking; *c)* fibre tensile failure; *d)* fibre compressive failure

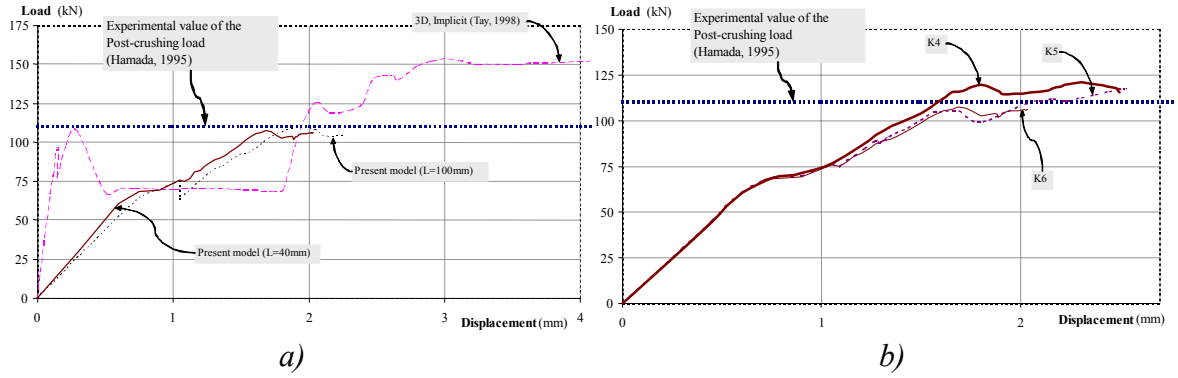

Figure 9: a) Comparison of the present results with the the numerical results from Reference [21]; b) effect of te penalty value (experimental post-crushing load from [23])

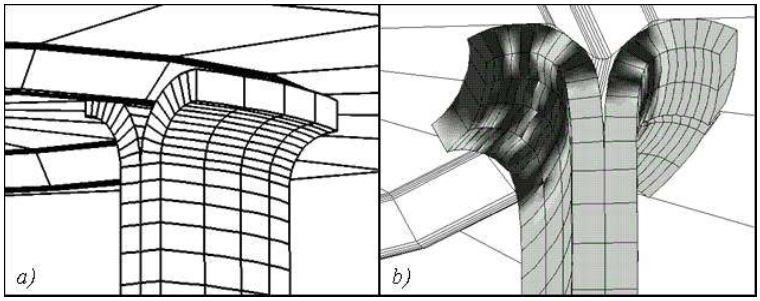

Figure 10: *a)* Finite element mesh for Case 1; *b)* damage ploted on the deformed mesh (the dark zones are damaged, according to the Mohr-Coulomb criterion)

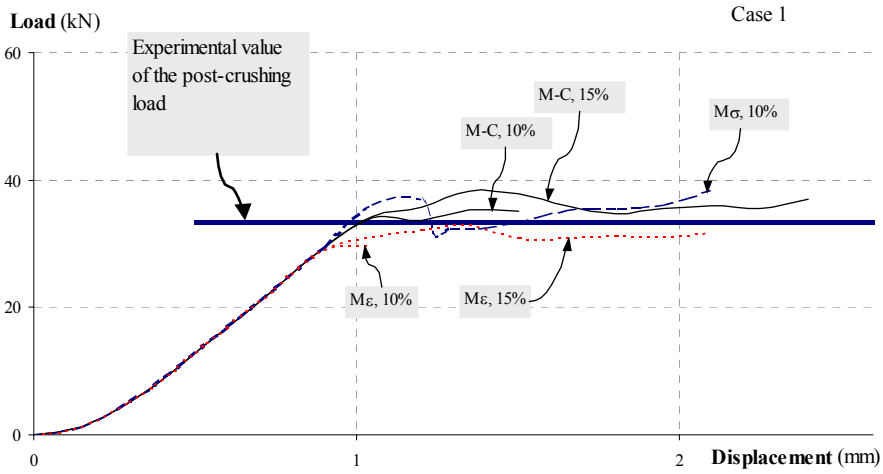

Figure 11: Present numerical results for Case 1, and comparison with the experimental post-crushing load from Reference [24]

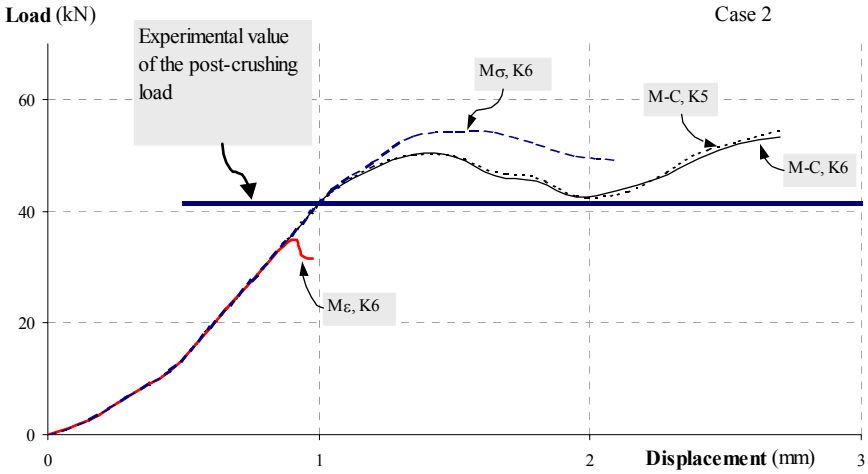

Figure 12: Present numerical results for Case 2, and comparison with the experimental post-crushing load from Reference [24]

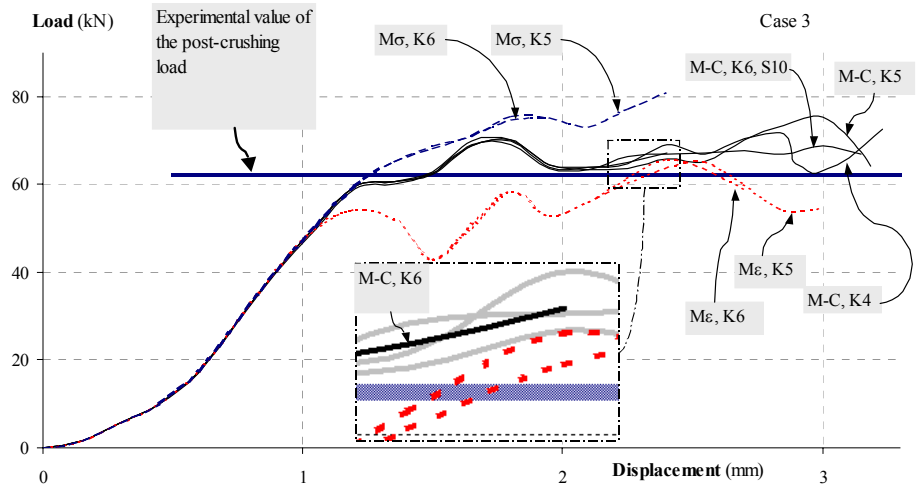

Figure 13: Present numerical results for Case 3, and comparison with the experimental results from Reference [24]

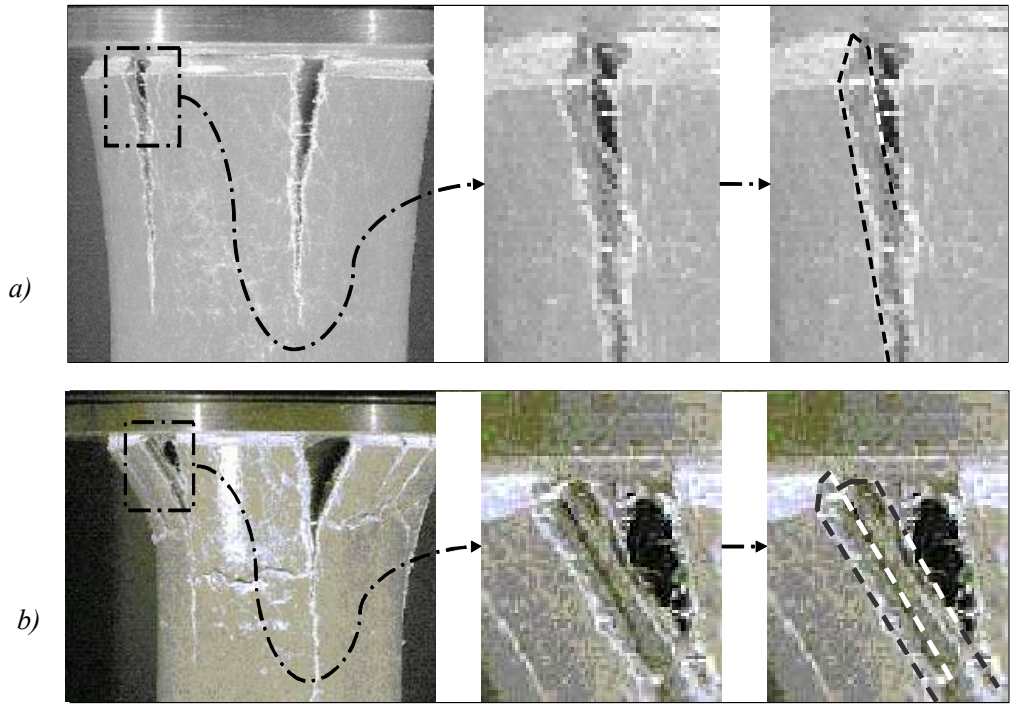

Figure 14: *a)* Detail showing the crushing of the inner-top edge during the initial; *b)* delamination of the wall. Original fotographs from Abdel-Haq *et al.* [25]

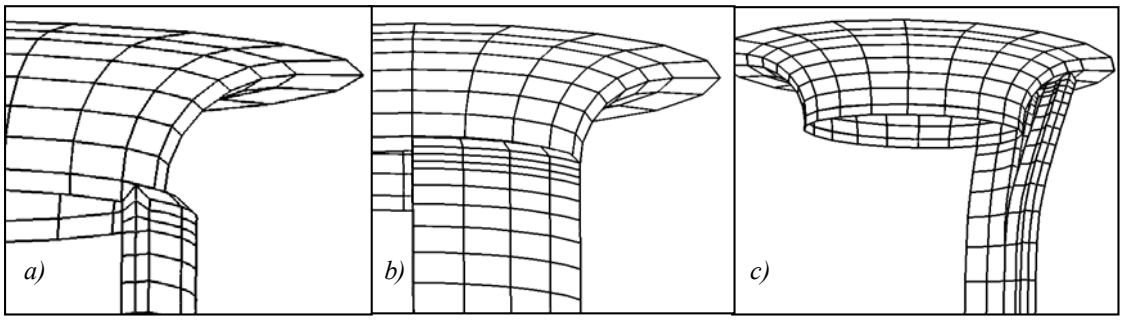

Figure 15: Mesh for the model corresponding to the tests by Abdel-Haq *et al.* [25]. In *a)* and *b)* not-deformed, and in *c)* deformed

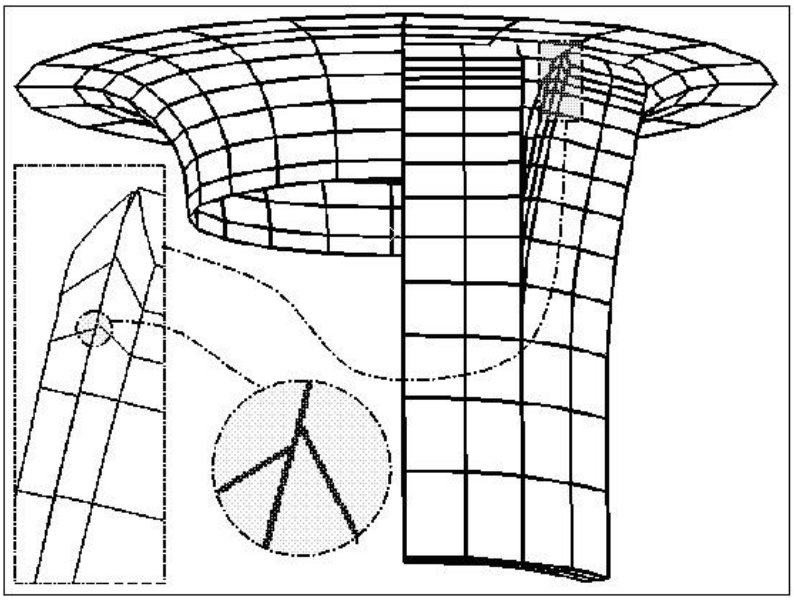

Figure 16: Deformed mesh of the model corresponding to the tests by Abdel-Haq *et al* [25]

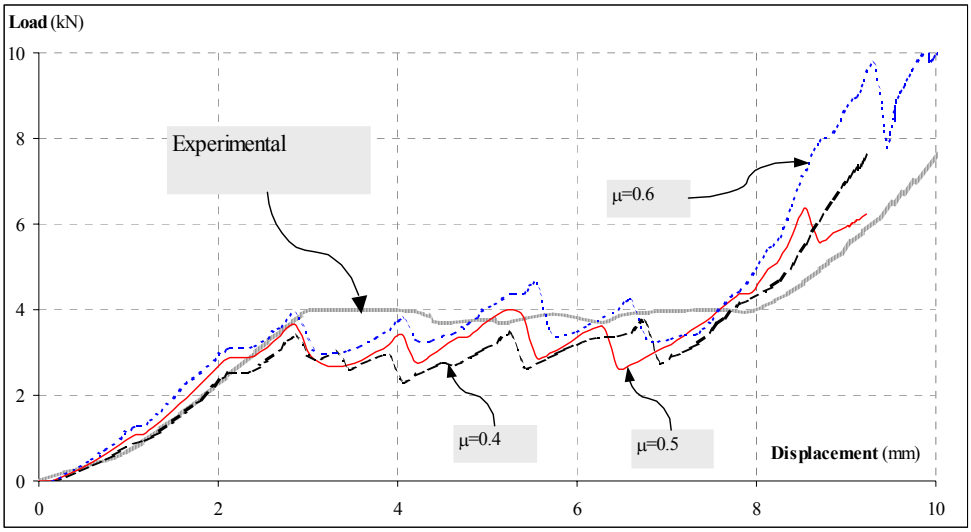

Figure 17: Numerical results with different friction coefficients, and comparison with Abdel-Haq *et al.* [25].